Evaluation of Automatic Landmark Selection Strategies for Navigation of Unmanned Aircraft

Nikolaus Ammann
German Aerospace Center (DLR)
Institute of Flight Systems
38108 Braunschweig, Germany
+49 531 295-2922
nikolaus.ammann@dlr.de

***Abstract*—This paper presents an extension of an approach for integrating pan-tilt camera systems into the state estimation of unmanned aircraft, thereby introducing an additional source of navigation data. The state estimation algorithm, based on a Unscented Kalman Filter (UKF), and the measurement model are presented in order to provide motivation for the presented landmark selection strategies. A variety of landmark selection strategies are put forth for consideration. Some are founded upon heuristic methodologies, while one employs the concept of the UKF by minimising state variance through the anticipation of potential landmark measurements. In order to evaluate the efficacy of the proposed strategies, a Matlab/Simulink simulation environment has been developed. This environment provides a range of measurements, including data from inertial, magnetic and barometric sensors, as well as emulated landmark tracking data. The subsequent section presents the evaluation of the various landmark selection strategies based on the mean position error over a range of different parameter sets. Finally, an outlook on prospective flight tests employing an unmanned helicopter weighing 85 kg is provided.**

TABLE OF CONTENTS

1. INTRODUCTION

Most current navigation systems for unmanned aircraft systems (UASs) rely on the fusion of inertial navigation systems (INS) and global navigation satellite systems (GNSS) [1]. A degradation or failure of GNSS signals, without additional redundant sensor data, will cause a divergence in the navigation state, leading to a violation of the UAS's navigation performance criteria. These performance criteria are defined by four key factors: accuracy, integrity, continuity, and availability [2] & [3]. The likelihood of GNSS signal degradation, due to both unintentional and intentional radio frequency interferences (RFIs), is high [4]. As a result, safe operation of autonomous systems such as UASs is not feasible under these conditions without redundancies in the navigation system [5]. To enhance navigation performance, data from other sensors such as barometers and magnetometers are commonly integrated into the fusion process. In addition, visual sensors like cameras are increasingly being used to estimate the navigation state in many commercially available UASs [6]. However, visual navigation remains an active area of research [7] & [8]. These navigation cameras serve a specific function and are mounted in fixed positions on the unmanned aerial vehicle (UAV). Their mounting locations and other system parameters, such as a wide field of view (FOV), are optimized for navigation purposes.

979-8-3503-5597-0/25/$31.00 ©2025 IEEE

Figure 1: Experimental sensor setup mounted to the payload bracket of DLR's unmanned research helicopter in a pivotable manner using a pan-tilt unit (PTU). The setup consists of two cameras with different focal lengths for landmark identification and tracking and a light detection and ranging (LiDAR) sensor for range measurements.

Camera systems supporting mission-specific tasks as part of the UAV's payload, are usually mounted on pivotable platforms and feature narrow or adjustable FOVs. Reconnaissance, surveillance, or surveying operations in both military and civilian applications make use of such camera systems. In these scenarios, high-resolution camera systems are needed, with a FOVs that can be directed toward specific areas of interest or targets, independent of the UAV's orientation. This allows for a wide field of regard (FOR), which represents the total area the pivoting camera can cover and is generally much larger than the FOV. Additionally, variations in the FOV caused by adjustments in focal length, and thus scene magnification, are particularly relevant when there is a considerable distance between the UAV and the target. These payload camera systems, along with their optics, tend to be of much higher quality compared to the integrated navigation camera systems [6] & [9].

Figure 1 depicts an experimental sensor setup mounted to the payload bracket of DLR's unmanned research helicopter

in a pivotable manner using a pan-tilt unit (PTU). The setup consists of two cameras with different focal lengths for landmark identification and tracking and a light detection and ranging (LiDAR) sensor for range measurements.

As pointed out in previous research papers the use of such payload camera systems has been proven to be beneficial for landmark-based navigation of UAS [10]. This paper extends the research done in the last publication [10] by exploiting possible strategies on improving the angles of the FOV to optimize the navigation state estimate.

In the first part of this paper the measurement model for landmark-based navigation using a pivotable camera system based on an UKF is repeated to give a better understanding of the basic model, which is used in the FOV optimization. The second part of this paper explains how the selection of the FOV angles influence the state estimation. Furthermore, this paper gives more landmark selection strategies compared to [10], where the FOV was set to maximize the number of visible landmarks. The results compare the navigation accuracy of the strategy used in [10] to the other proposed methods. The results show that the landmark selection strategy has a great impact on optimizing the navigation state estimate. Finally, an outlook on real flight tests using DLR's 85 kg unmanned helicopter is given.

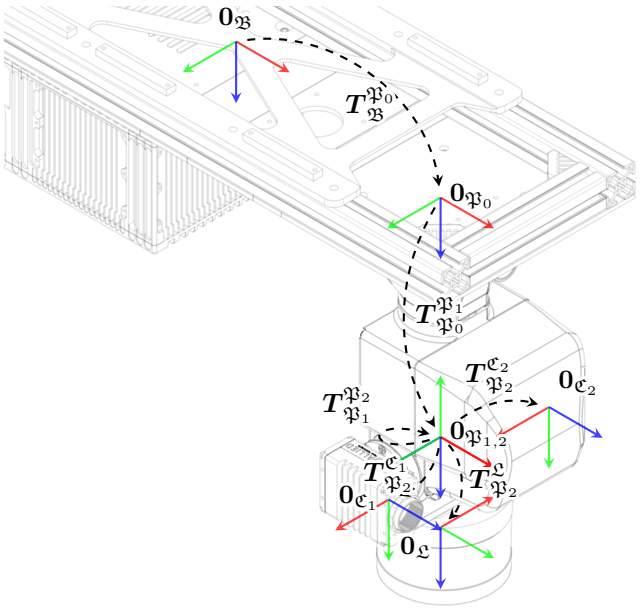

Figure 2: Kinematic chain with coordinate frames and transformations for the sensor setup used in the real system from figure 1 and in the simulation environment.

2. State Estimation

An integrated navigation system (INS) developed and presented in previous projects and papers [11] & [12] has been augmented in [10] with a specific measurement model to allow the fusion of a pivotable camera setup instead of a fixed camera setup. In this section the main characteristics of that INS are presented again for convenience. The INS combines high rate inertial navigation with low rate sensor fusion on a delayed time horizon. The sensor fusion algorithm is implemented using a low-rate error-state UKF.

The estimated error state is used to correct the propagated navigation solution from the inertial navigation. The UKF tracks the estimated error state $\delta\tilde{\boldsymbol{x}}_{k|k}$ of the system along with the corresponding variance $\boldsymbol{P}_{k|k}$ of that state [13] & [14]. In contrast to the original Kalman Filter (KF), the UKF uses nonlinear models for both the state transition and the measurement model. This allows more accurate processing of nonlinearities especially in the measurement model of image features. In this paper only the fundamentals of the UKF are presented shortly to introduce all necessary mathematical symbols. For a more detailed description of the INS including the process and measurement models of the UKF the reader is referred to [11] & [10].

The UKF uses deterministic sample points to approximate the distribution of the state. Therefore, a set of $2L+1$ so called sigma points $\boldsymbol{\chi}_{k|k}$ is drawn from the state $\delta\tilde{\boldsymbol{x}}_{k|k}$ and covariance $\boldsymbol{P}_{k|k}$, where $L = \dim(\delta\tilde{\boldsymbol{x}})$ is the dimension of the state. These sigma points $\boldsymbol{\chi}_{k|k}$ are propagated through the transition function $\mathrm{f} : \mathbb{R}^L \rightarrow \mathbb{R}^{\dim(\delta\boldsymbol{x})+\dim(\boldsymbol{z}_{k+1})}$. These transformed sigma points $\boldsymbol{\chi}_{k+1|k}$ are weighted and used to calculate the predicted state $\delta\tilde{\boldsymbol{x}}_{k+1|k}$ and covariance $\boldsymbol{P}_{k+1|k}$. For the update step of the UKF available measurements are fused in a batch as they become available. In this step the transformed sigma points $\boldsymbol{\chi}_{k+1|k}$ are projected through the observation or measurement function $\mathrm{h} : \mathbb{R}^{\dim(\delta\boldsymbol{x})+\dim(\boldsymbol{z}_{k+1})} \rightarrow \mathbb{R}^{\dim(\boldsymbol{z}_{k+1})}$ to calculate the so called gamma points $\boldsymbol{\gamma}_{k+1}$. These gamma points $\boldsymbol{\gamma}_{k+1}$ are again recombined to calculate the predicted measurement $\tilde{\boldsymbol{z}}_{k+1}$ and the predicted measurement covariance $\boldsymbol{P}_{z_{k+1},z_{k+1}}$. Furthermore, the gamma points $\boldsymbol{\gamma}_{k+1}$ as well as the transformed sigma points $\boldsymbol{\chi}_{k+1|k}$ are used for calculation of the state-measurement cross covariance matrix $\boldsymbol{P}_{x_{k+1},z_{k+1}}$. Finally, the Kalman gain matrix K_{k+1} is computed by using the predicted measurement covariance matrix $\boldsymbol{P}_{z_{k+1},z_{k+1}}$ and the state-measurement cross covariance matrix $\boldsymbol{P}_{x_{k+1},z_{k+1}}$. With all these auxillary variables the predicted state $\delta\tilde{\boldsymbol{x}}_{k+1|k}$ and covariance $\boldsymbol{P}_{k+1|k}$ can be updated and corrected using the provided measurements and form the next iteration of state $\delta\tilde{\boldsymbol{x}}_{k+1|k+1}$ and covariance $\boldsymbol{P}_{k+1|k+1}$.

The implemented low-rate error-state UKF fuses measurements from sensors, like IMU, altimeter, magnetometer, and barometer as well as landmarks and other features extracted from image data. By definition, landmarks have a known position in a reference coordinate frame and are identifiable in images. Examples of such landmarks are towers, wind turbines or other obstacles listed in airspace charts, where the position is known and the landmark can be identified with or without prior knowledge of the UAV's position and FOV. For specific scenarios however, fiducial markers like AprilTags [15], or ARTags [16] might also be used as valid landmarks. Therefore, in this paper, it is assumed that some sort of preprocessing system computes landmarks as a datum containing the image coordinates and the landmark identifier, corresponding to a position of that landmark in the reference coordinate frame. A detailed description of the measurement model is published in [10].

However, the measurement model depends on the kinematic chain visualized in figure 2 and expressed using the equations 1 and 2. The measurement is based on the current

position and attitude of the UAV, $\boldsymbol{r}_{\mathfrak{E}}$ and $\boldsymbol{R}^{\mathfrak{E}}_{\mathfrak{B}}$ respectively, as well as the position of a particular landmark i: $\boldsymbol{l}_{i,\mathfrak{E}}$.

$$\boldsymbol{l}_{i,\mathfrak{B}} = \left(\boldsymbol{R}^{\mathfrak{E}}_{\mathfrak{B}}\right)^{-1} \cdot (\boldsymbol{l}_{i,\mathfrak{E}} - \boldsymbol{r}_{\mathfrak{E}}) \tag{1}$$

$$\boldsymbol{l}_{i,\mathfrak{C}} = \boldsymbol{T}^{\mathfrak{C}}_{\mathfrak{P}_2} \cdot \boldsymbol{T}^{\mathfrak{P}_2}_{\mathfrak{P}_1} \cdot \boldsymbol{T}^{\mathfrak{P}_1}_{\mathfrak{P}_0} \cdot \boldsymbol{T}^{\mathfrak{P}_0}_{\mathfrak{B}} \cdot \boldsymbol{l}_{i,\mathfrak{B}} \tag{2}$$

Obviously, the perceived measurement depends on the UAV's position and attitude as well as the landmark's position. Additionally, the terms $\boldsymbol{T}^{\mathfrak{P}_1}_{\mathfrak{P}_0}$ and $\boldsymbol{T}^{\mathfrak{P}_2}_{\mathfrak{P}_1}$ in equation 2 depend on the current pan and tilt angles θ and γ of the PTU and thus influence the perception of a particular landmark.

By controlling the pan and tilt angles θ and γ of the PTU the system is able to influence the perceived measurements during the operation. As demonstrated in [10] the accuracy of the state estimation, particularly the mean position error, can be significantly reduced by leveraging a pivotable camera system for landmark based navigation of an UAV. In this paper different approaches for controlling θ and γ are evaluated.

3. LANDMARK SELECTION STRATEGIES

The objective of controlling the pan and tilt angles θ and γ of the PTU and thus the camera orientation is to improve the accuracy of state estimation by the navigation filter in comparison to a camera setup with a fixed orientation. To this end, a tracking algorithm was implemented to keep the selected landmark within the FOV of the camera over a specific time span or until the landmarks leaves the line of sight. The tracking of the landmark has been realized using a proportional-integral-derivative (PID) controller. The PID controller has two modes for tracking the landmark. One mode depends on the relative position of the landmark with repect to the UAV, leading to angle setpoints. The second mode belongs into the category of visual servoing algorithms, where the tracked landmark should be centered in the acquired images and the pixel offset corresponds to angular errors. Both control modes incorporate the relative motion of the landmark to the UAV and the angular motion of the UAV as an additional feedforward input. The controller calculates the angular velocity setpoints $\dot{\theta}$ and $\dot{\gamma}$ and sends these commands to the PTU. After the specific time span or after loss of the line of sight a different landmark is selected for tracking.

Different selection strategies of this landmark selection algorithm are proposed in this section. The different strategies can be divided into two classes with respect to the processing costs and the complexity of the algorithm. One class has low cost and low complexity and is referred to as to heuristics class. This class is intended rather for evaluation than actual operation. The more complex algorithms are based on the minimization of the state variance and are more computationally expensive.

Heuristics

Random selection of landmark— The random selection of a landmark for tracking is not a useful heuristic. Rather, the performance of this strategy can be used to estimate the minimum level of efficacy that another strategy or heuristic must attain in order to be deemed useful. Otherwise, the random selection and therefore no strategy would be more suitable than the strategy to be compared.

Minimal distance to landmark—The selection based on the minimal distance between the camera and the landmark is motivated based on the expected accuracy of the measurement. With a smaller distance the landmark is perceived as a larger patch in the image. Therefore, the perception of the landmark is considered to be more accurate and more reliable.

Maximize number of visible landmarks in FOV—It can be argued that the selection of a landmark with the largest number of neighbouring landmarks in the FOV is motivated by the fact that a larger number of measurement points is more likely to minimise the variance of the state estimate. However, the specific influence is due to the information contained in the measurement, and therefore this strategy can be considered a heuristic only. This strategy has been used in the previous publication [10] with the use of the pivotable camera system.

Minimization of the state variance

The UKF used in the state estimation module is a variant of the original KF. The KF is an optimal estimator in that it minimises the variance of the estimate on the basis of the available measurement data. This also provides the rationale for striving to minimise the state variance as a goal when selecting the camera's FOV. In combination with the feature tracking approach, the objective is therefore to identify the landmark whose positioning in the centre of the camera FOV minimises the expected state variance.

Firstly, the potential covariance matrices $\hat{\boldsymbol{P}}_{k+1|k+1}$ calculated by the UKF based on the current state $\delta\tilde{\boldsymbol{x}}_{k|k}$ and corresponding covariance $\boldsymbol{P}_{k|k}$ and all possible anticipated landmark measurements $\hat{\boldsymbol{z}}_{k+1}$ must be derived. Subsequently, the potential covariance matrices must be evaluated, with a variety of approaches available. The landmark resulting in the best rated potential covariance matrix is then selected for tracking in the next time span. These two aspects are discussed next.

For the calculation of the potential covariance matrices $\hat{\boldsymbol{P}}_{k+1|k+1}$ uses the UKF algorithm. Firstly, a set of sigma points $\boldsymbol{\chi}_{k|k}$ is drawn from the state $\delta\tilde{\boldsymbol{x}}_{k|k}$ and covariance $\boldsymbol{P}_{k|k}$. The following steps are performed for all landmarks from the catalog within a specific range. Subsequently, the signa points are projected through the measurement model h to form the anticipated gamma points $\hat{\boldsymbol{\gamma}}_{k+1}$ for one of the possible landmarks. The value of $\boldsymbol{l}_{i,\mathfrak{E}}$ in equations 1 of the measurement model is adjusted for each landmark i. For the terms $\boldsymbol{T}^{\mathfrak{P}_1}_{\mathfrak{P}_0}$ and $\boldsymbol{T}^{\mathfrak{P}_2}_{\mathfrak{P}_1}$ in equation 2 it is assumed that the angles θ and γ of the PTU are directly aligned with the direction of the landmark. This assumption is indeed valid, given that the PTU can be controlled by image-processing control algorithms, thereby ensuring that the object of interest is centered within the image. From the gamma points the predicted measurement $\tilde{\boldsymbol{z}}_{k+1}$ and corresponding measurement covariance $\boldsymbol{P}_{z_{k+1},z_{k+1}}$ can recombined. Since the real measurement is not known, the influence on the state is not predictable. But the predicted measurement covariance matrix $\boldsymbol{P}_{z_{k+1},z_{k+1}}$, which includes also the state uncertainty $\boldsymbol{P}_{k|k}$ as well as the measurement uncertainty $\boldsymbol{R}_{k+1}$, is valid under the assumption. Therefore, the update of the covariance matrices $\hat{\boldsymbol{P}}_{k+1|k+1}$ for any potential landmark measurement can be calculated.

After the potential covariance matrices $\hat{\boldsymbol{P}}_{k+1|k+1}$ for every possible anticipated landmark measurements $\hat{\boldsymbol{z}}_{k+1}$ have been calculated, the matrices have to be evaluated to select the one landmark resulting in the minimal state uncertainty. It is not possible to make a direct comparison between the covariance matrices that are anticipated for the potential measurements, as they contain a number of values that are of varying significance. Instead, a scalar is required that is capable of quantifying the quality of the measurement, and for which the value can be directly compared with that of other measurements.

The existing literature on the subject presents two principal methodologies for the comparison of covariance matrices:

Minimize the trace—The trace of a square matrix $\boldsymbol{P}$, denoted $\mathrm{tr}\,(\boldsymbol{P})$, is defined to be the sum of elements on the main diagonal. The trace as a scalar gives a measure of the total variance of the covariance matrix. Minimization of the trace of $\boldsymbol{P}$ is optimal in terms of the Kalman filter, which also leads to variance minimization [17] & [18]. It is acknowledged that a potential limitation of this methodology is that the variances represented in the covariance matrix are weighted differently according to the orders of magnitude and scales of the various variables involved [19].

Minimize the determinant— A comparable methodology is the calculation of the determinant of the covariance matrix $\det\,(\boldsymbol{P})$ as a scalar for the purpose of comparing the covariance matrices. This describes the volume of the so-called confidence ellipsoid, which accounts for the dependencies between the different variables of the error state, which are neglected in $\mathrm{tr}\,(\boldsymbol{P})$. Furthermore, the influence of different orders of magnitude on the result is reduced, as the strength of the influence of one variable on the volume of the ellipsoid also depends on the characteristics of the other variables [19].

With these two methodologies for comparing covariance matrices and the three described heuristics a set of five different landmark selection strategies have been proposed. In the following sections the evaluation process of these strategies is discussed.

4. SIMULATION FRAMEWORK

For testing and evaluation of the proposed landmark selection strategies the simulation environment used in previous research topics has been reused [10]. This simulation environment is capable to simulate measurements of sensors typically used in an UAV like an inertial measurement unit (IMU), a GNSS receiver, a magnetomater and a barometer. Moreover, the simulation environment must be capable of emulating optical sensor data. In order to derive quantifiable results from the simulation, the simulation is set up as a Monte Carlo simulation. For a given set of parameters, the simulation is initiated on multiple occasions. Furthermore, specific parameters are iterated over pre-defined values in order to evaluate the effect of these parameters on the output of the simulation. For example, the accuracy, integrity, continuity, and availability of each simulated sensor can be adjusted during the simulation to observe the consequences to the estimated state. This simulation setup has already been used in other UAV-based projects [20] but also for validation of lunar landing scenarios [21] & [22].

An important part of the simulation environment is the handling of the camera sensor. In this work the image acquisition, landmark identification, and landmark tracking is handled in the Tracking Emulator module. Typically, rendering of images has a high demand regarding the computational power. Furthermore, the images do not only depend on the sensor characteristics and the geometry of the environment but also on conditions like texture, lighting, and precipitation, which are highly dependend on the scenario and environment. The final step of the image processing pipeline would be the extraction of image features such as landmarks from the rendered images. These extracted image feautes contain only some image coordinates and some uncertainty values. Therefore, the complete pipeline of rendering of the image data, the feature and landmark extraction, and tracking has been emulated using statistical error models and phenomenological models for landmark identification and tracking algorithms [10]. This reduces the computational effort significantly. Based on the position and attitude of the UAV, the mounting position of the camera system, and the camera parameters the landmarks are projected into the camera frame. For the landmarks, which are within the field of view of the camera, the distance and assumed size of the landmark, which has also been extracted from the provided wind turbine data, defines the size in the image. From the set of visible landmarks with sufficient image size a subset is selected for further tracking, with a defined number of pixel separation. The landmarks for the subset are selected randomly, but already tracked landmarks are kept. The emulated tracked features and landmarks are prone to noise, drift, mismatches, and tracking losses. Each feature or landmark is further initialized with a tracking quality to incorporate the quality of an identified feature or landmark. This quality the integrated into the different random distributions used to independently configure all phenomenological error models.

Using this emulation of the complete image acquisition, landmark identification, and landmark tracking pipeline has shown realistic tracking performance based on evaluation of experts in the field. A more detailed description can be found in [10].

As mentioned earlier the simulation environment is set up as a Monte-Carlo simulation. This allows the evaluation of multiple simulation runs for a given set of parameters. Aditionally, specific parameters are iterated over pre-defined values in order to evaluate the effect of these parameters on the output of the simulation. Therefore, the important parameters for the simulation runs are documented in this paragraph. Especially, the iterated parameters are described.

Each simulation run simulates a time period of $300\,\mathrm{s}$. During the first $45\,\mathrm{s}$ the state estimation uses sensor measurements from the IMU, magnetometer, barometer, GNSS receiver, and the camera system. After that time period the GNSS receiver is disabled to simulate a loss of GNSS. The time period is choosen to allow a conversion of the UKF. After the initialization phase the state estimation depends only on the measurements of the camera system.

For the IMU, magnetometer, barometer, and GNSS receiver parameters are choosen to correspond to typical component of the self components. The camera system is parameterized as a simple megapixel camera. The focal length and therefore the FOV used in the simulation is one of the parameter changing during the simulation runs. The focal length is changed in the range of $8\,\mathrm{mm}$ to $16\,\mathrm{mm}$. This represents a minor modification of the parameter range in comparison with the preceding study [10]. The rationale for this adjustment is that the mean position error increases at the boundaries of

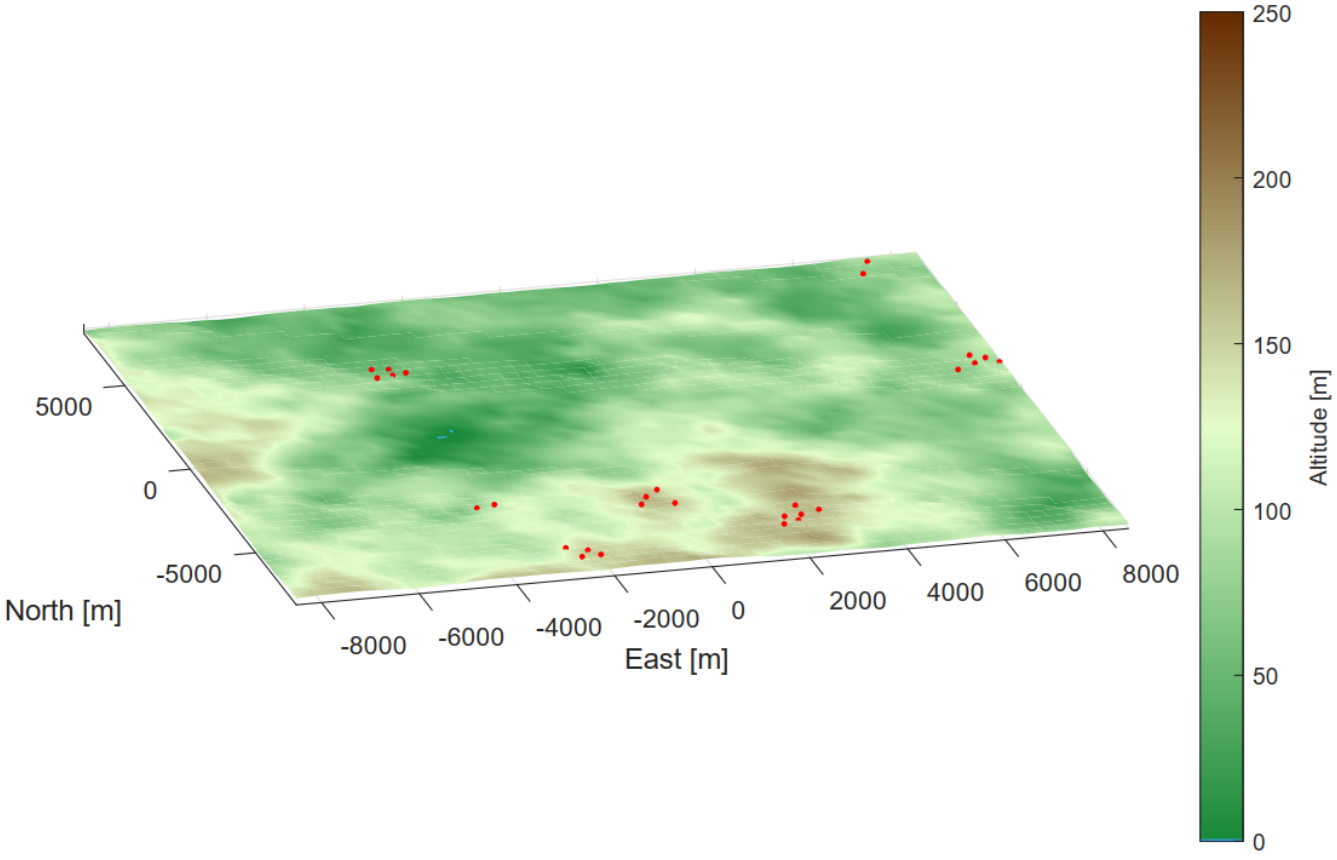

Figure 3: Visualization of the randomly generated elevation model and the distribution of landmarks.

the specified range, as previously outlined. Consequently, the range is reduced while maintaining the four samples to prioritise the relevant range. The camera system is mounted to a PTU as depicted in figure 1. This PTU is configured to have an angular range in the pan axis of $-120°$ to $120°$ and $-90°$ to $30°$ in the tilt axis. The mounting position of the camera system, which is defined by the setting of the PTU angles, is evaluated by either selecting static camera angles or actively adjusting the FOV during the simulation. The angular resolution of the real PTU is $0.06°$, while in simulation this parameter is changed from $0.01°$ to $0.1°$ between runs to evaluate the required accuracy of the PTU in this approach.

The scenario and the environment of the operation also have a huge influence on the density and visibility of the landmarks. Therefore, the environment is randomly generated for each of the simulation runs. This allows the generalization of the simulation results. Figure 3 shows an example of such a generated map containing an random elevation model with a number of random landmarks. The dimension of the map is derived from the generated flight geometry to allow a certain vertical buffer between the flight geometry and the end of the generated map. The elevation of the map is generated using Perlin noise, which is a commmon technique used in procedural game terrain generation [23]. A landmark is typically a recognisable natural or artificial object that emerges from its immediate surroundings and is often visible from considerable distances. For illustrative purposes, one might consider wind turbines as an example of such landmarks. These objects are included in official ICAO maps for both navigation and obstacle avoidance purposes. Therefore, the distribution of the landmarks in this simulation are based on the distribution of wind turbines in the northern part of Germany. The geographic positions of the registered wind turbines have been analysed to identify statistical measures to randomly generate realistic landmark distributions in the simulation environemnt. By using a clustering algorithm the mean and standard deviation of the number of landmarks per cluster, the spread of the clusters and the cluster density have been identified.

Finally, the landmark selection strategy used in the PTU controller is iterated between the simulation runs. In section 3 three heuristics and two methods for minimization of the state variance have been described. All of these five strategies are iterated over in the simulation to allow a detailed evaluation of the performance of each of these strategies.

5. Evaluation

To evaluate the simulation results the position error of the state estimation is visualized in different settings.

First, the error plots for all Monte-Carlo runs for an arbitrary parameter configuration are shown in figure 4. The plots show the errors of each simulation run, the calculated mean position error, and the 3σ bounds over time. It should be noted that the initialization phase is partially hidden for the sake of better visualization. Additionally, the error plots are also represented as box plots. These plots give an impression

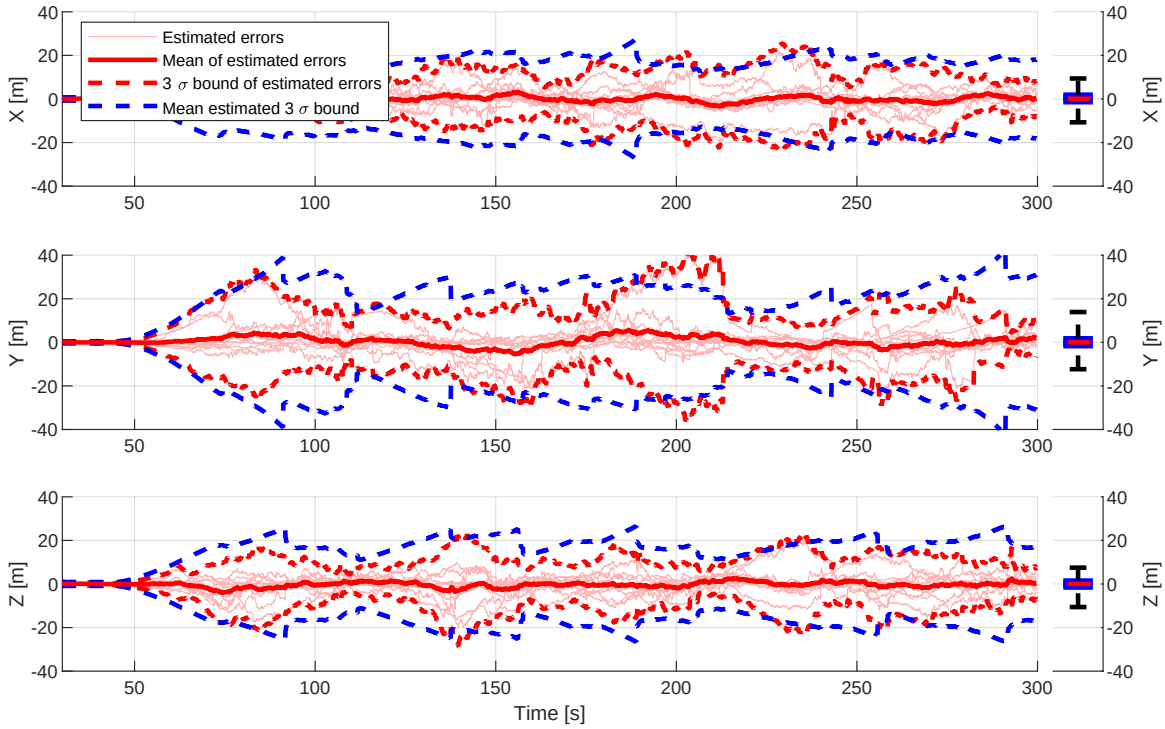

Figure 4: Error plot of the estimated position for each axis. The plots show the errors of each simulation runs for a defined parameter set, the calculated mean position error, and the 3σ bounds over time. Additionally, the error plots are also represented as box plots.

on how the state estimation performs generally during the simulation runs. During the initialization phase the position error and corresponding uncertainty converge to a value close to the correct value. After the first $45\,\mathrm{s}$ the GNSS updates are not available anymore to the state estimation, but a possible position drift and increase of the uncertainty cannot be observed due to the fusion of landmark measurements.

The preceding study demonstrated that the utilisation of an actively controlled camera system resulted in a notable enhancement in position accuracy when compared to a fixed camera system [10]. This conclusion is supported by the matrix plot presented in figure 5, which is again included in this paper for the reader's convenience. This plot shows the mean position error of all simulation runs for a fixed parameter set, encoded using a color based on the color bar, where blue is a small and red is a big error. The left matrix shows the results for a rigidly mounted camera system and the right matrix shows the results for a pivotable camera system. In this case the landmark selection strategy for maximizing the number of visible landmarks has been used. The variations in the focal length of the camera system are displayed on the horizontal axis, while the different angular resolutions or uncertainties are shown on the vertical axis. A detailed discussion on the impact of focal length and, consequently, the FOV changes as well as the angular resolution of the PTU on the mean position error has been presented in the previous paper [10].

The purpose of presenting figure 5 is to facilitate an analysis of the impact of varying landmark selection strategies. The matrix plot is calculated for all variations of landmark selection strategies. These plots are organized in the subsequent figure 6 in a new matrix structure, with the strategies arranged in rows and columns. The cells in this matrix represent the direct comparison of two specific strategies, with the basis for this comparison being the matrix plot from figure 5. The colours indicate the relative performance of the strategies in comparison. The parameter combinations for which a strategy performs best (red arrowhead pointing upwards) or worst (blue arrowhead pointing downwards) compared to all others are marked on the diagonal.

For each of the proposed strategies figure 6 presents some interesting findings:

- A random landmark selection strategy has been found to demonstrate mediocre performance. In the case of low PTU resolution and focal length, this strategy demonstrated the best performance compared to the other strategies presented. However, it also exhibited the worst performance when similar parameter sets were used.
- The heuristic based on the landmark with minimal distance to the camera demonstrates the poorest performance in comparison to all other selection strategies. Due to the UAV's changing position during flight, the landmark with minimal distance may be subject to temporal variation. However, it cannot be guaranteed that this strategy will select landmarks from different clusters. It is possible that the strategy will only consider landmarks from one single cluster, which is closest to the current position. This behaviour limits the information gain.
- The method of selecting the landmark with the highest number of visible neighbouring landmarks also exhibits mediocre performance. It is hypothesised that this inferior performance

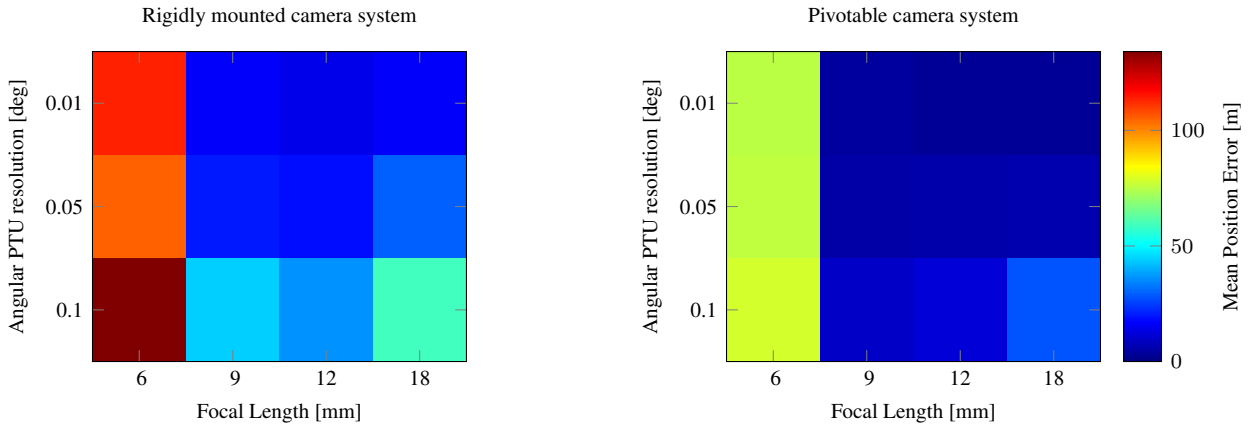

Figure 5: Matrix plots showing the mean position error of the two different camera mounting strategies from the previous paper. The amount is encoded using a color based on the color bar, where blue is a small and red is a big error. The variations in the focal length of the camera system are displayed on the horizontal axis, while the different angular resolutions or uncertainties are shown on the vertical axis.

is due to the strategy's tendency to focus on a single cluster of landmarks with minimal spread. This results in a greater number of landmark measurements, but the direction of these measurements with respect to a fixed coordinate frame remains unchanged. Consequently, there is an increase in uncertainty regarding the direction of the line of sight.

- It is evident that minimising the state variance's trace is not as effective as anticipated. The findings indicate two sets of parameters at which the strategy exhibits superior performance compared to other algorithms. However, there are also four instances where the strategy demonstrates the poorest performance.
- The landmark selection strategy minimizing the determinant of the state covariance matrix performs best. Given that the landmark has already been selected in a manner that minimises variance, the subsequent measurements serve to reduce the state variance as anticipated. This reduction in the confidence ellipsoid of the state covariance yields enhanced estimation accuracy, as evidenced by the results. This strategy has been demonstrated to achieve the most accurate position estimates in nearly all parameter sets, with the exception of those with low angular PTU resolution.

The findings demonstrate that the selection of landmarks for a pivotable camera system exerts a considerable impact on the attainable navigation performance, particularly in regard to the mean position error. The quality of landmark measurements, rather than the number of measurements themselves, has been demonstrated to exert a greater influence on the accuracy of state estimation. In this regard, the evaluation of measurement quality is inherently linked to the assessment of state estimation covariance.

6. Conclusion

This paper continues the research on active landmark-based navigation system using a PTU mounted camera system onboard UASs. These camera systems are part of the UAV's payload and thus serve to fulfill the mission and are typically not integrated into the avionics. However, these payload camera systems including the installed optics are typically of much higher quality than the integrated navigation camera systems.

This paper presents a number of different landmark selection strategies for a pivotable camera system. The described strategies have been tested and evaluated using the aforementioned simulation environment, which facilitates Monte Carlo simulations and allows for the variation of different parameter sets. The results demonstrate a notable enhancement in the precision of state estimation, not only due to the use of an actively controlled camera system in stead of a fixed camera system, but also highlight the significance of the optimal selection of perceived landmarks. It has been demonstrated that the minimisation of state variance through the selection of landmarks based on anticipated measurements yields superior results compared to the utilisation of straightforward heuristics, such as the maximisation of the number of visible landmarks within the FOV.

The described methods will be tested next onboard DLR's 85 kg unmanned helicopter. Therefore, the experimental setup as shown in figure 1 has already been set up and the flight test area has been prepared with fiducial markers as landmarks. The flight test results will be employed to validate the simulation environment, thereby enabling the generalization of the simulation results obtained.

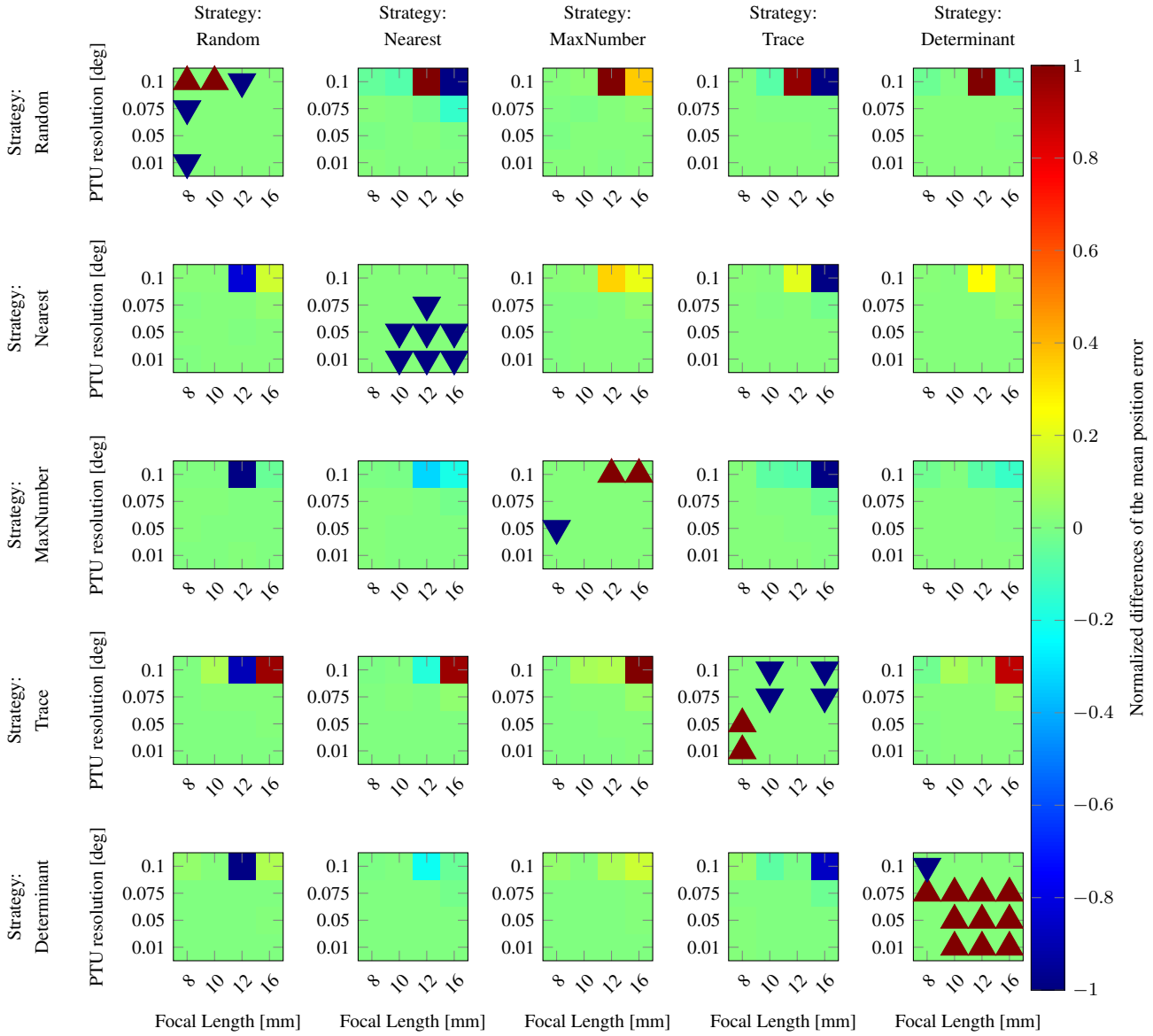

Figure 6: The figure depicts the normalized differences of the mean position error with the various strategies for each parameter combination. The colours indicate the relative performance of the strategies in comparison. The parameter combinations for which a strategy performs best (red arrowhead pointing upwards) or worst (blue arrowhead pointing downwards) compared to all others are marked on the diagonal.

REFERENCES

[1] K. P. Valavanis and G. J. Vachtsevanos, Eds., *Handbook of Unmanned Aerial Vehicles*. Springer Dordrecht, 2015.

[2] S. Gleason and D. Gebre-Egziabher, *GNSS Applications and Methods*. Artech House, 2009.

[3] H. Dodel and D. Häupler, *Satellitennavigation*. Springer, 2010.

[4] A. Hansen, S. Mackey, H. Wassaf, V. Shah, E. Wallischeck, C. Scarpone, M. Barzach, and E. Baskerville, "Complementary PNT and GPS Backup Technologies Demonstration Report Sections 1 through 10," 2021. [Online]. Available: https://www.transportation.gov/administrations/assistant-secretary-research-and-technology/complementary-pnt-and-gps-backup

[5] P. Leman, K. Gill, and M. Merkle, "Concept of Operations for NextGen Alternative Position, Navigation, and Timing (APNT)," 2012. [Online]. Available: https://www.faa.gov/sites/faa.gov/files/about/office_org/headquarters_offices/ato/20120319_APNT_CONOPS_FINAL.pdf

[6] DJI, "Matrice 300 RTK Benutzerhandbuch," 2022. [Online]. Available: https://dl.djicdn.com/downloads/matrice-300/20200717/M300_RTK_User_Manual_DE_0717.pdf

[7] Y. Lu, Z. Xue, G.-S. Xia, and L. Zhang, "A survey on vision-based UAV navigation," vol. 21, no. 1, 2018, pp. 21–32.

[8] M. Y. Arafat, M. M. Alam, and S. Moh, "Vision-Based Navigation Techniques for Unmanned Aerial Vehicles: Review and Challenges," vol. 7, no. 2, 2023, p. 89.

[9] Kappa optronics. (2023) Piloting Cameras für UAV & VTOL. [Online]. Available: https://www.kappa-optronics.com/de/aviation/uav-kameras/

[10] N. Ammann, "Active landmark navigation using a pan-tilt sensor system for unmanned aircraft," in *2024 IEEE Aerospace Conference*, 2024, pp. 1–8.

[11] N. Ammann and F. Andert, "Visual Navigation for Autonomous, Precise and Safe Landing on Celestial Bodies using Unscented Kalman Filtering," in *2017 IEEE Aerospace Conference*, 2017, pp. 1–12.

[12] F. Andert, N. Ammann, J. Püschel, and J. Dittrich, "On the Safe Navigation Problem for Unmanned Aircraft: Visual Odometry and Alignment Optimizations for UAV Positioning," in *2014 International Conference on Unmanned Aircraft Systems (ICUAS)*, 2014, pp. 734–743.

[13] S. Julier, J. Uhlmann, and H. Durrant-Whyte, "A new approach for filtering nonlinear systems," in *Proceedings of 1995 American Control Conference - ACC'95*, vol. 3. American Autom Control Council, 1995, pp. 1628–1632.

[14] S. Julier and J. Uhlmann, "New extension of the Kalman filter to nonlinear systems," in *Defense, Security, and Sensing*, 1997.

[15] E. Olson, "AprilTag: A robust and flexible visual fiducial system," in *2011 IEEE International Conference on Robotics and Automation*. IEEE, 2011, pp. 3400–3407.

[16] M. Fiala, "ARTag, a fiducial marker system using digital techniques," in *2005 IEEE Computer Society Conference on Computer Vision and Pattern Recognition*, vol. 2, 2005, pp. 590–596 vol. 2.

[17] Y. Bar-Shalom, X.-R. Li, and T. Kirubarajan. John Wiley & Sons, Inc., 2002.

[18] H. W. Sorenson, "Least-squares wstimation: From gauss to kalman," *IEEE Spectrum*, vol. 7, no. 7, pp. 63–68, 1970.

[19] C. Hajiyev and U. Hacizade, "Testing the Determinant of the Innovation Covariance Matrix Applied to Aircraft Sensor and Actuator/Surface Fault Detection," in *Advances in Sustainable Aviation*, T. H. Karakoç, C. O. Colpan, and Y. Şöhret, Eds. Springer International Publishing, 2018, pp. 269–283.

[20] F. Andert, N. A. Ammann, and M. Laubner, "Camera-Lidar Navigation for Large Unmanned Aircraft: Modular System Design and Safe Closed-Loop Testing Methodology," 2017.

[21] S. Theil, N. Ammann, F. Andert, T. Franz, H. Krüger, H. Lehner, M. Lingenauber, D. Lüdtke, B. Maass, C. Paproth, and J. Wohlfeil, "ATON (Autonomous Terrain-based Optical Navigation) for exploration missions: recent flight test results," vol. 10, no. 3, 2018, pp. 325–341.

[22] N. Ammann and L. García Mayo, "Undelayed Initialization of Inverse Depth Parameterized Landmarks in UKF-SLAM with Error State Formulation," in *2018 IEEE/ASME International Conference on Advanced Intelligent Mechatronics (AIM)*, 2018, pp. 918–923.

[23] T. J. Rose and A. G. Bakaoukas, "Algorithms and Approaches for Procedural Terrain Generation - A Brief Review of Current Techniques," in *2016 8th International Conference on Games and Virtual Worlds for Serious Applications (VS-GAMES)*, pp. 1–2.

BIOGRAPHY

Nikolaus Ammann *received his B.Sc. degree in computer science from the University of Lübeck in 2009. After his study abroad at the Auckland University of Technology in 2010 he graduated from the University of Lübeck in 2012 and received the M.Sc degree. Since then, he works as a research scientist at the German Aerospace Center (DLR). His research activities include sensor fusion and visual navigation for unmanned aerial vehicles (UAVs) and spacecraft.*